This ICCV paper is the Open Access version, provided by the Computer Vision Foundation.
Except for this watermark, it is identical to the accepted version;
the final published version of the proceedings is available on IEEE Xplore.

3D Test-time Adaptation via Graph Spectral Driven Point Shift

Xin Wei Qin Yang Yijie Fang Mingrui Zhu Nannan Wang✉
State Key Laboratory of Integrated Services Networks,
School of Telecommunications Engineering, Xidian University
{weixin, mrzhu, nnwang}@xidian.edu.cn {qinyang, fangyijie}@stu.xidian.edu.cn

Abstract

While test-time adaptation (TTA) methods effectively address domain shifts by dynamically adapting pre-trained models to target domain data during online inference, their application to 3D point clouds is hindered by their irregular and unordered structure. Current 3D TTA methods often rely on computationally expensive spatial-domain optimizations and may require additional training data. In contrast, we propose Graph Spectral Domain Test-Time Adaptation (GSDTTA), a novel approach for 3D point cloud classification that shifts adaptation to the graph spectral domain, enabling more efficient adaptation by capturing global structural properties with fewer parameters. Point clouds in target domain are represented as outlier-aware graphs and transformed into graph spectral domain by Graph Fourier Transform (GFT). For efficiency, adaptation is performed by optimizing only the lowest 10% of frequency components, which capture the majority of the point cloud's energy. An inverse GFT (IGFT) is then applied to reconstruct the adapted point cloud with the graph spectral-driven point shift. This process is enhanced by an eigenmap-guided self-training strategy that iteratively refines both the spectral adjustments and the model parameters. Experimental results and ablation studies on benchmark datasets demonstrate the effectiveness of GSDTTA, outperforming existing TTA methods for 3D point cloud classification.

1. Introduction

Point cloud classification is a fundamental area within computer vision, with a wide range of applications such as autonomous driving, virtual and augmented reality, and archaeology. Numerous deep models [1–13] have recently been developed for point cloud classification, demonstrating impressive performance. However, their success heavily relies on the oversimplified i.i.d. assumption for training and test data, overlooking the challenges of out-of-distribution scenarios that are frequently encountered in real-world applications. As illustrated in Fig. 1, a powerful point cloud classification deep model, DGCNN [2], trained on a clean dataset (ModelNet40 [14]), suffers a significant performance drop (over 35%) when tested on point clouds with real-world noises (*e.g.*, Background, Occlusion, and LiDAR corruptions). These corruptions are inevitable, arising from factors such as scene complexity, sensor inaccuracies, and processing errors, which hinders the practical deployment of these models.

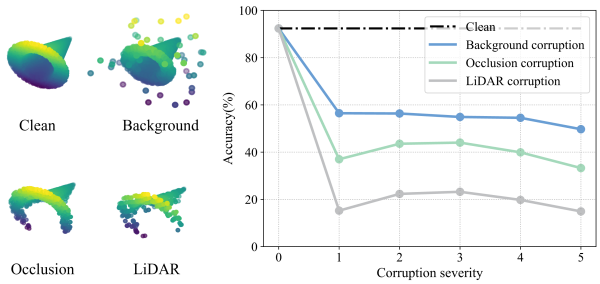

Figure 1. A point cloud classification model (DGCNN [2]), when trained on a clean dataset, suffers a significant performance drop when tested on point clouds with domain shifts.

Test-time adaptation (TTA) is a technique that enables models trained on the source domain to dynamically adapt to the target domain during online inference, showing significant promise in addressing domain shifts for 2D vision tasks [15–29]. At test time, TTA methods typically adapt either model parameters [15–22, 24, 26–29] or test data representations [23, 25] to reduce the gap between the training and test data distributions, improving performance on specific test samples. However, the irregular and unordered nature of 3D point clouds limits the direct application of 2D TTA methods to the 3D domain.

While recent studies have begun exploring TTA for 3D point clouds, the field remains in its early stages. MATE [30] introduces an auxiliary self-supervised reconstruction task during source domain training to improve robustness. Alternatively, BFTT3D [31] reduces error accumulation during adaptation by combining source-specific features with domain-independent ones from a non-

parametric network, but requires extracting feature prototypes from source domain data first. Both CloudFixer [32] and 3DD-TTA [33] leverage a diffusion model [34–36], pre-trained on source data, to repair corrupted point clouds by aligning them with the source distribution. However, both of these works do not strictly adhere to the test-time adaptation setting since they require access to source training data, which is often inaccessible in real-world applications. Moreover, MATE [30], CloudFixer [32] and 3DD-TTA [33] rely on the challenging optimization tasks of masked patch reconstruction or per-point transformation learning ($\Delta P \in R^{N\times 3}$ of a point cloud, where N often exceeds 1024). These high-dimensional optimization problems become particularly challenging when working with limited or streaming test data.

Unlike previous 3DTTA methods that adapt point clouds in the spatial domain, this work shifts the focus to adapting in the graph spectral domain at test time based on two key observations. First, spectral-based point cloud descriptors [37–43] leverage spectral analysis techniques from graph theory to capture the underlying structure and intrinsic geometric properties of point clouds. These spectral characteristics provide higher-level, global information, which encodes abstract, essential contexts crucial for point cloud recognition. Adjusting low-frequency components in the graph spectral domain requires approximately 90% fewer parameters than in the spatial domain to control a point cloud's global information, thus reducing optimization complexity with limited test data. Second, graph Laplacian eigenmaps serve as domain-independent descriptors, enabling robust adaptation. These eigenmaps complement the source-specific features extracted from the pre-trained model, which is especially valuable during the early stages of test-time adaptation before the model has fully adjusted to the target domain.

Along this idea, we propose a novel Graph Spectral Domain Test-Time Adaptation (GSDTTA) model for 3D point cloud classification. Given a point cloud classification model pre-trained on source domain data and a batch of test point clouds, GSDTTA adapts the input by operating within the graph spectral domain. Point clouds are represented as outlier-aware graphs and transformed into the spectral domain via the Graph Fourier Transform (GFT). A learnable spectral adjustment is then applied to the low-frequency components of each point cloud. The adjusted GFT coefficients are transformed back to the spatial domain using the inverse GFT (IGFT), resulting in a graph spectral-driven point shift. To optimize this process, we introduce an eigenmap-guided self-training strategy to generate pseudo-labels. This strategy guides the iterative optimization of both the spectral adjustment and the model parameters, progressively refining the adaptation. Extensive experiments on the ModelNet40-C [44] and ScanObjectNN-C [30] benchmarks confirm the effectiveness of our approach, with GSDTTA achieving significant performance gains over comparable methods.

Our contributions can be summarized as follows. First, we empirically demonstrate that the graph spectral domain of point clouds can capture global structural properties with fewer parameters and provide domain-independent features that facilitate robust cross-domain adaptation at test time. Second, we propose a novel graph spectral domain test-time adaptation model for 3D point cloud classification, featuring an eigenmap-guided self-training strategy for guiding the iterative optimization of spectral adjustments and model parameters. Third, our method achieves state-of-the-art 3D test-time adaptation performance on various benchmarks.

2. Preliminary and Motivation

2.1. Problem Definition

In the context of 3D test-time adaptation, we consider a point cloud classification model $f_\theta(\cdot)$ trained on a source dataset $\mathcal{D}_S = \{\mathcal{X}, \mathcal{Y}\}$ inaccessible at test time. Each point cloud $X \in \mathcal{X}$ is represented as a set of three-dimensional vectors $X = \{x_i\}_{i=1}^N$, following the distribution $p(\mathcal{X})$, and f_g denotes the global deep descriptor of the point cloud extracted by model f_θ. Given an unlabeled target dataset $\mathcal{D}_T = \{\tilde{\mathcal{X}}\}$, where each point cloud $\tilde{X} \in \tilde{\mathcal{X}}$ is drawn from a different distribution $q(\mathcal{X}) \neq p(\mathcal{X})$, the objective of test-time adaptation is to enable accurate predictions despite these distribution shifts. Test-time adaptation achieves this by adapting model parameters θ [19, 21, 30, 31, 45], the target data $\tilde{X}$ [23, 25, 32], or prompts in transformer-based models [24, 46, 47]. Current approaches typically adapt one or a combination of these components in an online or batch-wise manner during inference, without requiring extensive access to target data at each test step.

2.2. Graph Spectral Analysis for Point Clouds

Given a point cloud $X \in \mathbb{R}^{N\times 3}$ with N points, an undirected graph $G = (V, A)$ is built with i-th node v_i as the i-th point x_i in point cloud X. The element A_{ij} of adjacency matrix $A \in R^{N\times N}$ is defined as:

$$A_{ij} = \mathbb{I}(x_j \in \mathcal{N}(x_i)), \tag{1}$$

where $\mathbb{I}(\cdot)$ is a binary function indicating whether x_j is within the kNN of x_i in spatial domain. The combinatorial graph Laplacian matrix of G is then computed by:

$$L = D - A, \tag{2}$$

where D is the diagonal degree matrix with $D_{i,i} = \sum_{j=1}^N A_{ij}$. Since L is a real, symmetric and positive semi-positive matrix, the Laplacian eigenvector matrix $U = [u_1, u_2, ..., u_N]$ and the eigenvalue matrix $\Lambda =$

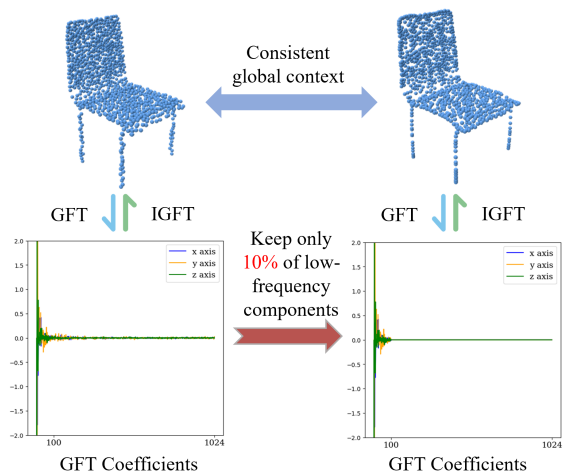

Figure 2. Analysis of a chair point cloud's graph spectrum shows that 95% of the spectral energy is concentrated in the low-frequency components, and that the lowest 10% of these components are sufficient to reconstruct its global shape.

$diag([\lambda_1, ..., \lambda_N])$ are computed by eigen decomposition:

$$L = U\Lambda U^T. \tag{3}$$

In this decomposition, each eigenvector u_i in U is orthogonal to the others, and the eigenvalues λ_i in Λ satisfy the ordering condition $\{\lambda_1 = 0 \leq ... \leq \lambda_i \leq \lambda_{i+1} \leq ... \leq \lambda_N\}$. The eigenvalues of a graph are referred to as the graph frequency or spectrum of a point cloud, with larger eigenvalues corresponding to higher graph frequencies. The eigenmaps are subspaces of eigenvectors, constructed by excluding the eigenvector associated with the eigenvalue of 0, and using the remaining m eigenvectors to embed the graph nodes into an m-dimensionals space $E : v_i \rightarrow [u_1(v_i), ..., u_m(v_i)]$. We can derive a global spectral descriptor f_s for the point cloud by applying element-wise max-pooling to the embedded features of the graph nodes, which is a simplified variant of the well-known Global Point Signature [40]:

$$f_s = \text{maxpooling}(E(v_1), ..., E(v_m)). \tag{4}$$

The spectral coefficients of any vertex v_i of G is derived by:

$$\hat{v}_i = \phi_{\text{GFT}}(v_i) = U^T v_i. \tag{5}$$

The inverse Graph Fourier Transform (IGFT) transforms the spectral coefficients to spatial domain:

$$v_i = \phi_{\text{IGFT}}(\hat{v}_i) = U\hat{v}_i. \tag{6}$$

2.3. Motivation on 3D Test-time Adaptation via Graph Spectral Driven Point Shift

As introduced in Sect. 1, our method adapts point clouds in the graph spectral domain. We motivate this choice by two key properties of this domain, which we then experimentally validate: it efficiently captures global structure with few parameters, and its features are domain-independent, providing a robust complement to potentially source-biased deep features.

The graph spectral domain exhibits remarkable efficiency and invariance. First, as illustrated in Fig. 2, it demonstrates strong energy compaction, with about 95% of a chair point cloud's spectral energy concentrated in its low-frequency components (typically 100 coefficients). This allows us to reconstruct the global context using only the lowest 10% of coefficients, significantly simplifying the optimization process compared to adapting features in the spatial domain. This is especially beneficial for online or data-limited TTA. Second, the low-frequency eigenmap provides an isometrically invariant shape descriptor that is inherently domain-agnostic. This contrasts sharply with deep features, which often retain source-domain bias, especially early in adaptation. Our ablation studies confirm that augmenting deep features with these stable spectral descriptors enhances adaptation performance.

Capitalizing on these properties, we introduce a graph spectral driven point shift for adaptation. Our method applies a learnable spectral adjustment directly to the low-frequency components of each test point cloud. To optimize this adjustment and the model parameters θ, we employ an eigenmap-guided self-training strategy. This strategy generates high-quality pseudo-labels by forming a convex combination of logits derived from two complementary sources: the global deep descriptors and the robust, domain-independent global spectral descriptors.

3. Method

In this section, we introduce the framework for the Graph Spectral Domain Test-Time Adaptation (GSDTTA) model. As shown in Fig. 3, GSDTTA comprises two main components: Graph Spectral Driven Point Shift (GSDPS) and Graph Spectral Guided Model Adaptation (GSGMA). The input point cloud X and the point cloud classification model f_θ are iteratively adapted by GSDPS and GSGMA, progressively refining the adaptation process at test time.

3.1. Graph Spectral Driven Point Shift

In the Graph Spectral Driven Point Shift (GSDPS) model, each input point cloud is adapted through a point shift derived from graph spectral adjustment. A point cloud is initially constructed as an outlier-aware graph, transformed into the graph spectral domain, and adjusted in its low-frequency components via a spectral adjustment. The adjusted spectral representation is then converted back to the spatial domain, resulting in a point cloud with a graph spectral driven point shift. The spectral adjustment is optimized through an eigenmap-guided self-training strategy.

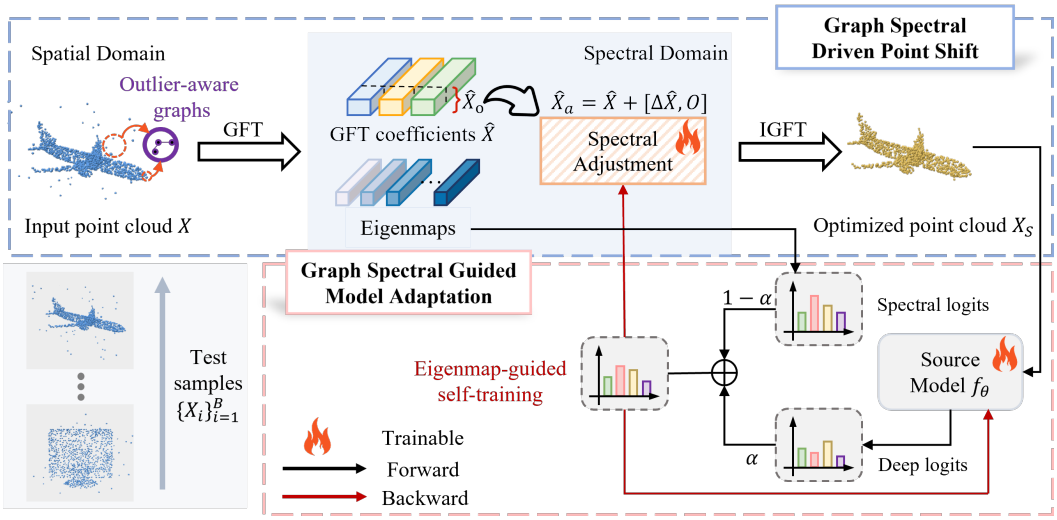

Figure 3. The pipeline of the proposed GSDTTA. Given a batch of test samples $\{X_i\}_{i=1}^B$ and point classification model f_θ pre-trained on source domain, Graph Spectral Driven Point Shift (GSDPS) and Graph Spectral Guided Model Adaptation (GSGMA) modules iteratively adapt both the point cloud and model in the graph spectral space. This adaptation is achieved by optimizing the spectral adjustment $\Delta\hat{X}$ and model parameters θ through an eigenmap-guided self-training strategy.

From point clouds to outlier-aware graphs. Given a point cloud $X \in \mathbb{R}^{N\times 3}$, we first construct a graph $G_o = \{V, A_o\}$ upon X. We use Radial Basis Function (RBF) as the weight function for the edges between points x_i and x_j:

$$w_{ij} = exp(-\frac{d^2(x_i, x_j)}{2\delta^2}), \tag{7}$$

where $d(\cdot,\cdot)$ denotes the squared Euclidean distance between two vertices and δ is a hyperparameter. The element of the adjacency matrix A is then given by:

$$A_{ij} = w_{ij} \cdot \mathbb{I}(x_j \in \mathcal{N}(x_i)), \tag{8}$$

where $\mathbb{I}(\cdot)$ is an indicator function where edges are only kept if x_j is within the k-NN neighborhood $\mathcal{N}(x_i)$.

Since spectral analysis of point cloud graphs can be sensitive to outliers, we leverage the fact that outliers are often far from inlier points. As a result, the degree of outlier vertices—defined as the sum of weights on all adjacent edges—tends to be significantly lower than that of inlier points. Erroneous points can therefore be removed by eliminating vertices with degrees below a threshold τ. The element of final adjacency matrix A_o is defined as:

$$A^o_{ij} = w_{ij} \cdot \mathbb{I}(x_j \in \mathcal{N}(x_i)) \cdot \mathbb{I}(\sum_{j=1}^{N} A_{ij} > \tau), \tag{9}$$

The threshold τ is calculated as γ times the average k-nearest neighbor distance across the entire point cloud, providing a global measure of point dispersion:

$$\tau = \frac{\gamma}{Nk} \sum_{i=1}^{N}\sum_{j=1}^{N} A_{ij}. \tag{10}$$

Spectral adjustment driven point shift. The Laplacian matrix L_o of the outlier-aware graph G_o is computed by $L_o = D_o - A_o$ where D_o is the degree matrix, and then decomposed to obtain the eigenvector matrix U_o by solving $L_o = U_o \Lambda_o U_o^T$. These eigenvectors are used to compute the GFT coefficients as follows:

$$\hat{X} = U_o^T X, \tag{11}$$

where $\hat{X} \in \mathbb{R}^{N\times 3}$ represents the transformed coefficients of signal in the three axes. Then a learnable spectral adjustment $\Delta\hat{X} \in R^{M\times 3}, M << N$ is deployed to adjust the coefficients $\hat{X}$ of low frequency:

$$\hat{X}_a = \hat{X} + \Delta\hat{X}', \tag{12}$$

where $\Delta\hat{X}' = [\Delta\hat{X}, O] \in R^{N\times 3}$ is defined as the concatenation of $\Delta\hat{X} \in R^{M\times 3}$ and a zero matrix $O \in R^{(N-M)\times 3}$. Finally, the adjusted spectral representation $\hat{X}_a$ is converted back to the spatial domain to obtain the point cloud with a graph spectral driven point shift:

$$X_s = U_o \hat{X}_a. \tag{13}$$

The spectral adjustment $\Delta\hat{X}$ will be optimized automatically according to the objective function that will introduced in following section.

Optimizing spectral adjustment by Eigenmap-guided self-training. To optimize the spectral adjustment $\Delta\hat{X}$, as discussed in Sect. 2.3, we propose an eigenmap-guided self-training strategy to generate pseudo-labels for self-supervised training. Given a batch of point clouds $\{X_i\}_{i=1}^B$

with global deep descriptors $\{f_d^i\}_{i=1}^B$ and global spectral descriptors $\{f_s^i\}_{i=1}^B$, the centroids q_d^c for c-th class in the global deep descriptor space are defined as:

$$q_d^c = \frac{\sum_{i=1}^B (f_\theta(X_i))_c f_d^i}{\sum_{i=1}^B (f_\theta(X_i))_c}, \tag{14}$$

where $(f_\theta(X_i))_c \in R$ is the class probability for the c-th class of the target sample X_i. Similarly, the centroids q_s^c in the global spectral descriptor space are defined as:

$$q_s^c = \frac{\sum_{i=1}^B (f_\theta(X_i))_c f_s^i}{\sum_{i=1}^B (f_\theta(X_i))_c}. \tag{15}$$

The centroids q_d^c and q_s^c serve as soft cluster assignments for class c, providing robust representations to guide adaptation. The final pseudo-label $\hat{y}_i$ for test sample X_i is generated as a convex combination of the class probabilities of f_d^i and f_s^i:

$$\hat{y}_i = \arg\min_c (\alpha \frac{(f_d^i)^T q_d^c}{\|f_d^i\| \|q_d^c\|} + (1-\alpha) \frac{(f_s^i)^T q_s^c}{\|f_s^i\| \|q_s^c\|}), \tag{16}$$

where α is a weight factor to balance the two terms. The overall input adaptation objective is:

$$\arg\min_{\Delta\hat{X}} \mathcal{L}_{IA} = \arg\min_{\Delta\hat{X}} (\mathcal{L}_{pl} + \beta_1(\mathcal{L}_{ent} + \mathcal{L}_{div}) + \beta_2 \mathcal{L}_{cd}), \tag{17}$$

where $\mathcal{L}_{pl} = CE(f_\theta(X_s), \hat{y})$ is the cross entropy loss. $\mathcal{L}_{ent}$ denotes the entropy loss as $-\sum_{c=1}^C f_\theta(X_s) \log f_\theta(X_s)$, which encourages the model to make more confident predictions on the optimized point cloud. Divergency loss $\mathcal{L}_{div} = \sum_{c=1}^C g_c \log(g_c)$, where $g_c = \frac{1}{B} \sum_{i=1}^B (f_\theta(X_i))_c$, promotes diversity in the outputs while ensuring individual certainty. Together, $\mathcal{L}_{ent}$ and $\mathcal{L}_{div}$ form an information maximization loss [48, 49]. $\mathcal{L}_{cd}$ is the single direction Chamfer Distance from input point cloud X to adapted point cloud X_s, encouraging X to be a part of X_s. β_1 and β_2 are weight factors controlling the relative contributions of different losses.

3.2. Graph Spectral Guided Model adaptation

To optimize the model's adaptation to the target domain, we apply graph spectral-guided model adaptation to adjust the parameters θ of the point cloud classification model f_θ. The objective function of model adaptation is:

$$\arg\min_\theta \mathcal{L}_{MA} = \arg\min_\theta (\mathcal{L}_{pl} + \beta_3(\mathcal{L}_{ent} + \mathcal{L}_{div})), \tag{18}$$

where $\mathcal{L}_{pl}$, $\mathcal{L}_{ent}$, and $\mathcal{L}_{div}$ are the same losses defined in the input adaptation step. β_3 is a weight factor.

In GSDTTA, the input and model adaptations are optimized in an iterative manner to improve the point cloud classification model's performance under domain shifts. This process alternates between two steps: optimizing the spectral adjustment $\Delta\hat{X}$ for input adaptation and updating the model parameters θ for model adaptation. By iteratively refining both the point clouds and the model parameters, GSDTTA achieves better alignment between the test data and the pre-trained model, leading to enhanced classification accuracy when faced with challenging domain shifts.

4. Experiment

In this section, experiments are conducted on ModelNet40-C and ScanObjectNN-C benchmarks to verify the efficacy of the proposed GSDTTA.

4.1. Datasets

ModelNet40-C. ModelNet40[14] dataset is a 3D point cloud classification benchmark containing 12,311 shapes across 40 categories (9,843 for training, 2,468 for testing). From this, ModelNet40-C[44] benchmark was created to evaluate model robustness. It augments the original test set with 15 common, realistic corruptions organized into three categories: transformations, noise, and density variations. These corruptions simulate real-world distributional shifts, providing a rigorous test of model reliability. For further details, please refer to [44].

ScanObjectNN-C. ScanObjectNN [50] is a real-world point cloud classification dataset derived from scanned indoor scenes, comprising 15 object categories with 2,309 training samples and 581 testing samples. For consistent robustness evaluation, the ScanObjectNN test set is augmented with the same 15 corruption types applied in ModelNet40-C, forming the ScanObjectNN-C dataset [30].

4.2. Implementation Details

For experiments on the three benchmarks above, we use DGCNN [2], CurveNet [3], and PointNeXt [13] as the point cloud classification model f_θ across all comparable methods. For fair comparison, all methods use the same pre-trained weights of backbone networks for each dataset. We report results obtained by running the published code for each method, with detailed implementation information provided in the supplementary material.

As discussed in Sect. 3.2, for GSDTTA, input and model adaptations are optimized iteratively to enhance the robustness and performance of the point cloud classification model under domain shifts. For each batch of test data, GSDTTA first adapts the input point cloud over 4 steps, followed by 1 step of model adaptation, repeating this cycle for a total of 10 steps. The objective function in Eqn. 17 and Eqn. 18 for both stages is optimized using the AdamW optimizer [51], with a learning rate of 0.0001 and batch size of 32. The parameters k for k-NN,δ and γ for constructing the outlier-aware graph in Sect. 3.1 are set to 10, 0.1 and

Backbone	Method	uniform	gaussian	background	impulse	upsampling	rbf	rbf-inv	den-dec	dens-inc	shear	rot	cut	distort	occlusion	lidar	Mean
DGCNN [2]	Source-only	79.57	72.16	49.71	64.70	67.99	78.03	80.47	73.05	82.73	85.08	59.52	75.81	80.71	33.26	14.91	66.51
	BN [15]	84.48	82.82	48.01	81.32	79.98	81.68	83.22	78.36	86.10	85.53	72.24	81.23	82.90	41.12	31.11	73.34
	PL [45]	85.29	83.67	65.64	83.46	80.51	82.77	84.35	79.29	85.89	84.88	74.39	81.96	82.86	38.69	31.68	75.02
	DUA [22]	84.48	83.10	50.97	81.80	79.94	82.00	83.26	79.29	86.22	85.94	71.96	81.56	82.49	42.09	32.09	73.81
	TENT [16]	86.02	84.88	60.65	83.54	82.73	83.18	84.76	80.83	**87.19**	86.83	75.32	82.98	83.46	42.94	33.38	75.91
	SHOT [19]	85.69	83.95	81.40	84.19	82.21	82.86	83.75	79.86	85.25	84.35	77.95	82.41	83.95	**48.46**	34.11	77.36
	BFTT3D [31]	78.47	71.45	46.85	66.75	70.87	75.69	78.43	73.12	81.90	82.35	56.45	75.49	78.43	34.80	16.75	65.86
	CloudFixer [32]	**89.95**	**90.15**	74.55	**90.11**	85.98	82.13	84.81	73.46	84.76	82.70	77.67	76.74	81.65	35.94	**37.48**	76.54
	3DD-TTA [33]	85.58	84.00	62.48	76.13	**88.41**	78.36	80.59	73.30	84.85	82.74	59.93	72.77	79.34	38.41	28.48	71.69
	GSDTTA (ours)	87.88	86.26	**88.57**	86.91	84.12	**85.05**	**86.18**	**82.46**	86.83	**87.76**	**78.53**	**84.20**	**84.44**	45.38	31.52	**79.07**
CurveNet [3]	Source-only	88.13	84.76	15.56	65.56	89.10	85.49	86.18	78.81	87.97	87.20	70.83	78.44	86.63	36.06	29.98	71.38
	BN [15]	89.38	87.40	36.26	80.35	89.34	86.67	87.76	84.04	88.98	88.01	78.69	84.64	87.12	47.20	45.91	77.45
	PL [45]	89.26	88.45	36.43	83.87	88.86	87.68	**88.94**	85.29	89.30	88.74	82.70	87.03	87.44	47.33	47.12	78.56
	DUA [22]	89.30	87.40	36.26	80.27	89.38	86.63	87.68	83.91	89.02	87.97	78.48	84.56	87.12	47.12	45.98	77.41
	TENT [16]	89.42	87.56	36.63	81.48	89.47	87.28	87.68	84.48	88.94	88.25	79.42	85.41	87.12	48.14	46.88	77.88
	SHOT [19]	87.56	87.40	66.49	86.18	83.83	87.40	88.01	**85.78**	87.28	87.48	**83.95**	86.30	86.35	**58.63**	**56.04**	81.24
	BFTT3D [31]	85.63	81.86	16.07	66.64	89.26	84.60	84.93	79.25	87.79	86.36	68.18	79.45	86.15	37.13	30.96	70.95
	CloudFixer [32]	**90.14**	**89.98**	66.07	**90.06**	**90.87**	85.59	87.30	76.18	86.20	85.06	81.86	78.61	84.86	37.13	38.76	77.91
	GSDTTA (ours)	89.74	89.30	**87.84**	87.88	89.87	**88.53**	88.61	85.66	**89.55**	**89.22**	82.90	**87.20**	**87.97**	50.73	44.45	**82.63**
PointNeXt [13]	Source-only	69.12	57.86	50.81	70.62	77.03	75.04	77.55	86.18	87.84	79.01	42.50	85.82	76.46	41.05	27.96	66.99
	BN [15]	86.63	84.81	78.69	87.03	88.13	84.16	85.78	89.71	90.92	84.68	70.10	89.55	83.43	51.18	45.54	80.02
	PL [45]	87.15	85.13	78.89	87.93	86.79	85.01	**86.79**	89.10	90.03	86.06	77.76	88.70	84.85	51.62	46.35	80.81
	DUA [22]	87.32	85.37	79.78	87.88	88.45	84.72	86.18	**89.91**	90.76	84.72	72.16	89.34	83.58	51.94	46.39	80.57
	TENT [16]	87.80	86.43	80.43	88.25	88.70	85.05	86.30	89.38	**91.09**	85.37	74.59	**89.63**	84.32	51.90	46.92	81.08
	SHOT [19]	86.39	85.74	81.44	85.41	81.28	84.20	85.70	87.96	88.65	83.43	79.54	88.01	84.68	**55.43**	**49.03**	80.46
	BFTT3D [31]	70.17	61.24	54.22	73.13	78.25	75.81	77.72	87.18	88.76	80.36	43.71	86.97	77.52	42.45	28.41	68.39
	CloudFixer [32]	**87.91**	**88.32**	79.28	88.36	**88.98**	80.26	82.32	80.47	82.32	76.69	65.42	83.18	83.06	38.32	35.73	76.04
	GSDTTA (ours)	87.48	86.71	**91.29**	**88.81**	88.29	**85.82**	86.75	89.06	90.48	**86.06**	**80.06**	89.02	**85.98**	55.06	46.84	**82.51**

Table 1. Classification accuracy (%) is provided for each distribution shift in the ModelNet40-C dataset [44]. These results reflect the performance of backbone models trained on ModelNet40 [14] and adapted to the corrupted dataset using a batch size of 32. Source-only indicates the accuracy achieved on corrupted test data without applying any adaptation method. The mean accuracy scores are reported, with the highest values highlighted in bold and the second highest underlined.

0.6, respectively. In the graph spectral domain, the number of frequency components is set to $M = 100$, as defined in Eqn. 12. The weight factor α in Eqn. 16, β_1, β_2 in Eqn. 17 for input adaptation, β_3 for model adaptation in Eqn. 18 are set to 0.5, 0.3, 1000, 3 respectively. All experiments are conducted on a single NVIDIA RTX 3090 GPU.

4.3. Results

ModelNet40-C. Table 1 provides a detailed performance comparison of various TTA methods on the ModelNet40-C [44] dataset, featuring 2D TTA methods like BN [15], PL [45], DUA [22], TENT [16], and SHOT [19], along with 3D-specific TTA methods such as BFTT3D [31] and CloudFixer [32]. Our GSDTTA model achieves highest mean accuracy across all three backbones: 79.07% (DGCNN), 82.63% (CurveNet), and 82.51% (PointNeXt) and maintains the highest or the second highest performance under most corruption types. Compared to SHOT [19], the best-performing 2DTTA method, GSDTTA achieves improvements of 1.71%, 1.39%, and 2.05% on three backbones respectively, highlighting effectiveness of the special design of GSDTTA for 3D point cloud data. Additionally, GSDTTA achieves consistent improvements of 2.53% (DGCNN), 4.72% (CurveNet), and 6.47% (PointNeXt) over the previous state-of-the-art 3DTTA method CloudFixer [32]. Our method outperforms CloudFixer on 11 corruption types with DGCNN and CurveNet, and 12 types with PointNeXt. These improvements demonstrate the effectiveness of GSDTTA in adapting point clouds within the graph spectral domain at test time. The consistent gains across different backbones underscore GSDTTA's adaptability and efficiency, establishing it as a robust solution for 3D test-time adaptation in point cloud classification under a variety of challenging distribution shifts.

ScanObjectNN-C. We conducted additional experiments on the challenging real-scanned point cloud dataset ScanObjectNN-C [30] to further validate the effectiveness of GSDTTA. As shown in Table 2, the source models for each backbone achieve relatively low classification accuracies, underscoring a significant distribution shift between ScanObjectNN-C and its clean counterpart, ScanObjectNN [50]. GSDTTA demonstrates notable improvements over existing methods across all tested backbones. Specifically, it surpasses CloudFixer, which operates in the spatial domain using diffusion models, with accuracy gains of 1.10%, 3.63%, and 1.83% for three backbones respectively. It is worth nothing that CloudFixer outperforms our method on four basic noise-related corruptions (Uniform, Gaussian, Impulse, and Upsampling), with an average margin of 8.35% across the three backbones. This is expected since CloudFixer specifically leverages diffusion models' denoising capabilities. For high-level semantic corruptions, GSDTTA demonstrates better average results on part dropping (Shear: +4.68%, Cutout: +3.60%) under three backbones. This shows that the overall mean improvement (+2.19%) of GSDTTA comes from consistent performance across diverse corruptions. The better handling of semantic corruptions highlights the benefits of GSDTTA's graph spectral approach, which effectively captures global structural features with a reduced number of parameters. This design enables

Backbone	Method	uniform	gaussian	background	impulse	upsampling	rbf	rbf-inv	den-dec	dens-inc	shear	rot	cut	distort	occlusion	lidar	Mean
DGCNN [2]	Source-only	46.99	44.75	40.96	65.75	56.63	70.40	71.94	67.64	73.32	72.63	61.79	68.33	73.32	10.67	10.67	55.72
	BN [15]	56.28	52.66	25.47	67.81	62.13	**71.42**	73.67	69.01	74.35	73.67	66.78	70.56	**73.67**	9.98	9.81	57.15
	PL [45]	60.75	55.93	21.51	70.39	**67.12**	69.87	72.11	69.53	73.32	72.28	66.95	**71.42**	72.46	**11.18**	10.32	57.68
	DUA [22]	57.31	53.87	22.37	68.84	64.19	70.91	72.81	70.39	74.69	74.52	**67.12**	70.74	73.32	10.67	10.32	57.47
	TENT [16]	60.24	54.73	19.27	70.39	65.57	70.91	72.11	68.15	74.35	73.14	66.26	70.91	73.14	10.84	9.63	57.31
	SHOT [19]	59.89	59.04	17.21	70.05	68.15	69.01	70.22	67.98	70.39	69.53	65.40	67.81	69.53	10.67	9.98	56.32
	BFTT3D [31]	48.96	48.96	41.32	66.84	58.68	71.18	72.57	67.88	72.05	73.96	61.98	68.75	72.92	10.24	**10.76**	56.47
	CloudFixer [32]	**71.70**	**68.92**	46.18	**75.00**	**72.92**	70.14	72.05	66.32	73.09	72.40	61.46	69.79	73.14	9.55	8.33	60.73
	3DD-TTA [33]	58.52	54.04	46.64	65.75	62.82	67.13	70.91	69.71	74.01	71.08	58.69	68.67	70.91	8.95	8.43	57.08
	GSDTTA (ours)	63.17	58.52	**69.54**	73.67	66.09	71.26	**74.01**	**70.74**	**75.04**	**74.87**	66.61	69.02	**73.67**	10.67	10.51	**61.83**
CurveNet [3]	Source-only	44.75	37.35	24.96	40.62	51.29	71.77	74.35	68.68	76.42	74.53	65.92	70.91	73.84	10.33	10.15	53.06
	BN [15]	56.28	50.26	27.19	54.04	62.99	**72.29**	75.22	71.77	76.76	74.87	70.57	71.94	**75.22**	10.67	9.81	57.33
	PL [45]	62.99	52.67	30.12	58.86	62.65	70.22	74.01	72.29	75.04	75.04	71.26	71.08	72.98	10.15	9.12	57.90
	DUA [22]	60.58	55.07	28.05	57.83	64.37	70.57	75.73	**73.15**	76.42	75.56	71.26	71.94	74.87	10.50	9.29	58.35
	TENT [16]	62.13	55.94	29.43	58.52	64.89	70.91	75.73	72.98	76.76	75.56	71.94	71.43	74.35	10.84	9.29	58.71
	SHOT [19]	65.75	59.04	22.38	65.57	61.96	70.91	73.49	70.91	74.01	74.01	70.05	72.12	72.81	9.12	**10.50**	58.17
	BFTT3D [31]	50.87	42.01	25.35	43.06	54.51	69.62	73.44	64.76	69.62	71.53	66.32	62.85	73.44	**10.94**	10.24	52.57
	CloudFixer [32]	**69.79**	**68.58**	31.77	**75.00**	**70.14**	67.71	72.74	63.02	73.44	70.14	64.76	68.92	71.88	10.59	5.90	58.96
	GSDTTA (ours)	64.37	58.00	**67.13**	69.71	66.78	71.94	**75.90**	70.05	**77.12**	**76.08**	**72.12**	**73.67**	**75.22**	10.67	10.15	**62.59**
PointNeXt [13]	Source-only	32.70	23.58	39.41	46.82	44.06	68.67	69.36	73.49	74.53	70.40	55.25	73.32	71.43	9.12	7.75	50.66
	BN [15]	46.64	38.73	43.55	59.21	58.52	72.46	**74.01**	73.49	77.28	**72.46**	64.37	75.39	74.35	11.88	7.92	56.68
	PL [45]	53.01	42.17	39.41	60.59	60.24	72.29	71.60	73.32	75.04	69.02	64.03	73.49	70.05	**12.22**	9.64	56.41
	DUA [22]	51.81	43.37	41.13	63.34	62.99	**73.67**	73.15	73.32	**77.97**	71.94	66.78	75.56	**75.22**	12.05	9.64	58.13
	TENT [16]	53.87	44.23	41.14	63.86	62.31	72.98	72.46	72.81	77.11	70.74	**67.30**	75.39	73.67	11.88	**10.80**	58.05
	SHOT [19]	52.84	44.41	39.93	65.06	60.76	72.12	71.60	72.98	76.25	69.02	65.23	72.46	71.43	11.88	9.98	57.06
	BFTT3D [31]	33.51	24.48	39.93	47.40	44.79	69.10	69.79	**74.31**	74.83	71.01	54.86	73.78	71.70	9.20	7.81	51.10
	CloudFixer [32]	**65.28**	**63.72**	46.53	**79.51**	**78.30**	65.45	67.01	69.27	72.40	65.62	57.29	68.92	69.44	9.38	6.94	59.01
	GSDTTA (ours)	53.87	46.64	**69.88**	74.35	63.51	72.81	73.15	73.49	76.59	71.26	66.78	**75.73**	72.98	11.70	9.81	**60.84**

Table 2. Classification accuracy (%) across various distributional shifts in the ScanObjectNN-C dataset[30]. The results presented are based on three backbone models, each trained on the main split of the ScanObjectNN dataset [50] and subsequently adapted to the OOD test set with a batch size of 32. Mean accuracy scores are reported with the highest values highlighted in bold and the second highest underlined.

GSDTTA to handle complex distribution shifts more efficiently than traditional spatial domain adaptations, making it particularly suitable for robust 3D test-time adaptation under real-world challenges.

4.4. Ablation Study

In this section, we take a closer look at the effects of components of GSDTTA, including the Graph Spectral Driven Point Shift (GSDPS) module for input adaptation, Graph Spectral Guided Model Adaptation (GSGMA) module for model adaptation, and eigenmap-guided self-training strategy. All experiments are conducted on the Scanobjectnn-C dataset with DGCNN [2] as backbone network.

Effectiveness of components in GSDTTA. We conduct an ablation study to evaluate the impact of each component in the GSDTTA framework. First, we remove the GSDPS module for input adaptation, denoting this variant as GSDTTA (w/o GSDPS), where only the original point cloud is processed by the model f_θ and adapted using the GSGMA module with the eigenmap-guided self-training strategy. As shown in Table 3, GSDTTA improves mean accuracy by 4.55% over GSDTTA (w/o GSDPS) across 15 corruptions, demonstrating the effectiveness of GSDPS in adapting point clouds in the graph spectral domain. Next, we remove the GSGMA module, leaving only GSDPS adapt the input without model parameter updates, referred to as GSDTTA (w/o GSGMA). The full GSDTTA outperforms this variant by 3.48%, underscoring the importance of model adaptation with the eigenmap-guided self-training strategy. We also evaluate the impact of our outlier-aware graph by setting $\gamma = 0$ in Eq. 10. Without this component, accuracy on background corruption drops dramatically from 69.54% to 18.24%, while average accuracy on the other 14 corruptions remains similar (61.44% *vs.* 61.28%). This shows that the graphs are highly sensitive to outliers in background corruption, while the noises are easy to be remove.

To validate the eigenmap-guided self-training strategy, we generate three pseudo-label variants for some corruption types (Uniform, Background, Rotation, and Cutout). These pseudo-labels are obtained from clustering global deep descriptors, clustering global spectral descriptors, and the eigenmap-guided approach in Eqn.16. As shown in Fig. 4, eigenmap-guided pseudo-labels achieve superior performance on some corruptions with accuracy improvements compared to deep descriptor-based labels, validating our motivation presented in Sect. 2.3. To further investigate the role of eigenmaps, we replace GSDTTA's eigenmap-guided self-training strategy with a deep-feature-guided approach in Table 3, which generates pseudo-labels solely from global deep descriptors. The 0.63% performance degradation confirms the eigenmap's essential role as a domain-agnostic complement to source-specific features during initial adaptation.

Sensitivity analysis on the hyperparameters. We conduct an experiment on the ScanObjectNN-C dataset using DGCNN as the backbone model under shear corruption to analyze the sensitivity of weight factors β_1, β_2, and β_3 in the loss functions specified in Eqn. 17 and Eqn. 18. For each experiment, other hyperparameters are fixed as described in Sect. 4.2. As shown in Fig. 5, the classification accuracy

Table 3. Mean accuracy (%) of variants of GSDTTA for point cloud classification on ScanObjectNN-C with DGCNN.

GSDPS	GSGMA	EGSS	Mean
✗	✗	-	55.72
✗	✓	✓	57.28
✓	✗	✓	58.35
✓	✓	✗	61.20
✓	✓	✓	**61.83**

Figure 4. The classification accuracy of deep logits, spectral logits, and eigenmap-guided logits under some corruptions.

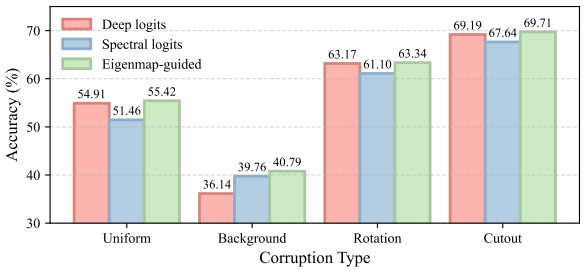

of GSDTTA remains stable with respect to β_1, β_2, and β_3 within the ranges of $[0, 1]$, $[0, 3000]$, and $[0, 5]$, respectively, with standard deviations of 0.27, 0.25, and 0.95. This indicates that GSDTTA is not sensitive to these weight factors within the tested ranges.

5. Related Work

Test-time adaptation. Test-time adaptation methods for 2D images have emerged as effective solutions to address challenges caused by domain shift, enabling models pre-trained on source domains to adapt dynamically to target domain data. For more details of 2D TTA methods, please refer to the supplementary materials. However, their applicability to 3D point cloud classification remains limited due to the unique challenges posed by irregular and unordered 3D data. MATE [30] addresses these challenges by employing masked autoencoders for self-supervised auxiliary tasks, enabling test-time adaptation to diverse point cloud distributions. BFTT3D [31] takes a different approach by introducing a backpropagation-free adaptation model to mitigate error accumulation. Cloudfixer [32] leverages pre-trained diffusion models for point cloud denoising before adapting the classification model. Similarly, 3DD-TTA [33] employs a diffusion model to adapt target data to the source domain while maintaining frozen source model parameters. In contrast, GSDTTA departs from spatial-domain methods by leveraging the graph spectral domain for efficient and robust adaptation. By optimizing low-frequency spectral components where most of the point cloud's global structural information resides, GSDTTA significantly reduces the number of parameters requiring adaptation.

Figure 5. Sensitivity analysis of hyperparameters β_1, β_2, and β_3 on ScanObjectNN-C dataset under shear corruption with DGCNN.

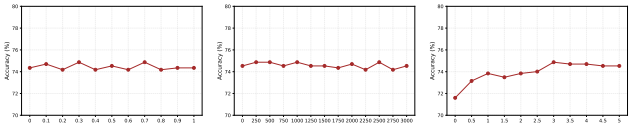

(a) β_1 (b) β_2 (c) β_3

Graph spectral analysis for point clouds. Just as frequency domain analysis enhances 2D vision models [52–54], spectral methods for point clouds excel at analyzing intrinsic geometric structure. In point cloud matching, spectral analysis techniques extract features that capture the underlying structure of point clouds [37–43]. A key principle of the graph spectral domain is that low-frequency components preserve global structure, while high-frequency components capture finer details and noise. Leveraging this, spectral filters have been developed for denoising [55, 56], while other methods manipulate Graph Fourier Transform (GFT) coefficients for attacks [57, 58] or robust contrastive learning [59]. Building on these strengths, our method, GSDTTA, adapts both point clouds and model parameters in the graph spectral domain. We leverage the global structural information in low-frequency components to enable efficient and robust adaptation to distribution shifts, significantly improving performance in 3D classification tasks.

6. Conclusion

We proposed GSDTTA, a novel graph spectral domain test-time adaptation model that uses an eigenmap-guided self-training strategy. Extensive experiments validate its effectiveness on standard 3D-TTA benchmarks. While GSDTTA excels on these benchmarks, its scalability to large-scale point clouds is currently limited by the computational complexity of global spectral operations. Future work will address this by exploring unsupervised segmentation and multi-scale local spectral analysis to improve efficiency and reduce computational costs.

Acknowledgment This work was supported in part by the China Postdoctoral Science Foundation under Grant Number 2025M771559, in part by the Postdoctoral Fellowship Program of CPSF under Grant Number GZB20250399, in part by the National Natural Science Foundation of China under Grants U22A2096 and 62036007, in part by Scientific and Technological Innovation Teams in Shaanxi Province under grant 2025RS-CXTD-011, in part by the Shaanxi Province Core Technology Research and Development Project under grant 2024QY2-GJHX-11, in part by the Fundamental Research Funds for the Central Universities under GrantQTZX23042, in part by the Young Talent Fund of Association for Science and Technology in Shaanxi China under Grant 20230121.

References

[1] Charles R Qi, Hao Su, Kaichun Mo, and Leonidas J Guibas. Pointnet: Deep learning on point sets for 3d classification and segmentation. In *CVPR*, pages 652–660, 2017. 1

[2] Yue Wang, Yongbin Sun, Ziwei Liu, Sanjay E Sarma, Michael M Bronstein, and Justin M Solomon. Dynamic graph cnn for learning on point clouds. *ACM TOG*, 38(5):1–12, 2019. 1, 5, 6, 7

[3] Tiange Xiang, Chaoyi Zhang, Yang Song, Jianhui Yu, and Weidong Cai. Walk in the cloud: Learning curves for point clouds shape analysis. In *ICCV*, pages 915–924, 2021. 5, 6, 7

[4] Charles Ruizhongtai Qi, Li Yi, Hao Su, and Leonidas J Guibas. Pointnet++: Deep hierarchical feature learning on point sets in a metric space. In *NeurIPS*, volume 30, 2017.

[5] Yongcheng Liu, Bin Fan, Shiming Xiang, and Chunhong Pan. Relation-shape convolutional neural network for point cloud analysis. In *CVPR*, pages 8895–8904, 2019.

[6] Meng-Hao Guo, Jun-Xiong Cai, Zheng-Ning Liu, Tai-Jiang Mu, Ralph R Martin, and Shi-Min Hu. Pct: Point cloud transformer. *CVM*, pages 187–199, 2021.

[7] Ankit Goyal, Hei Law, Bowei Liu, Alejandro Newell, and Jia Deng. Revisiting point cloud shape classification with a simple and effective baseline. In *ICML*, pages 3809–3820, 2021.

[8] Haoxi Ran, Wei Zhuo, Jun Liu, and Li Lu. Learning inner-group relations on point clouds. In *ICCV*, pages 15477–15487, 2021.

[9] Yangyan Li, Rui Bu, Mingchao Sun, Wei Wu, Xinhan Di, and Baoquan Chen. Pointcnn: Convolution on x-transformed points. In *NeurIPS*, volume 31, 2018.

[10] Xu Ma, Can Qin, Haoxuan You, Haoxi Ran, and Yun Fu. Rethinking network design and local geometry in point cloud: A simple residual mlp framework. In *ICLR*, 2022.

[11] Yifan Xu, Tianqi Fan, Mingye Xu, Long Zeng, and Yu Qiao. Spidercnn: Deep learning on point sets with parameterized convolutional filters. In *ECCV*, pages 87–102, 2018.

[12] Hugues Thomas, Charles R Qi, Jean-Emmanuel Deschaud, Beatriz Marcotegui, François Goulette, and Leonidas J Guibas. Kpconv: Flexible and deformable convolution for point clouds. In *ICCV*, pages 6411–6420, 2019.

[13] Guocheng Qian, Yuchen Li, Houwen Peng, Jinjie Mai, Hasan Hammoud, Mohamed Elhoseiny, and Bernard Ghanem. Pointnext: Revisiting pointnet++ with improved training and scaling strategies. In *NeurIPS*, volume 35, pages 23192–23204, 2022. 1, 5, 6, 7

[14] Zhirong Wu, Shuran Song, Aditya Khosla, Fisher Yu, Linguang Zhang, Xiaoou Tang, and Jianxiong Xiao. 3d shapenets: A deep representation for volumetric shapes. In *CVPR*, pages 1912–1920, 2015. 1, 5, 6

[15] Steffen Schneider, Evgenia Rusak, Luisa Eck, Oliver Bringmann, Wieland Brendel, and Matthias Bethge. Improving robustness against common corruptions by covariate shift adaptation. In *NeurIPS*, volume 33, pages 11539–11551, 2020. 1, 6, 7

[16] Dequan Wang, Evan Shelhamer, Shaoteng Liu, Bruno Olshausen, and Trevor Darrell. Tent: Fully test-time adaptation by entropy minimization. In *ICLR*, 2021. 6, 7

[17] Yusuke Iwasawa and Yutaka Matsuo. Test-time classifier adjustment module for model-agnostic domain generalization. In *NeurIPS*, volume 34, pages 2427–2440, 2021.

[18] Yige Yuan, Bingbing Xu, Liang Hou, Fei Sun, Huawei Shen, and Xueqi Cheng. Tea: Test-time energy adaptation. In *CVPR*, pages 23901–23911, 2024.

[19] Jian Liang, Dapeng Hu, and Jiashi Feng. Do we really need to access the source data? source hypothesis transfer for unsupervised domain adaptation. In *ICML*, pages 6028–6039, 2020. 2, 6, 7

[20] Marvin Zhang, Sergey Levine, and Chelsea Finn. Memo: Test time robustness via adaptation and augmentation. In *NeurIPS*, volume 35, pages 38629–38642, 2022.

[21] Jing Ma. Improved self-training for test-time adaptation. In *CVPR*, pages 23701–23710, 2024. 2

[22] M Jehanzeb Mirza, Jakub Micorek, Horst Possegger, and Horst Bischof. The norm must go on: Dynamic unsupervised domain adaptation by normalization. In *CVPR*, pages 14765–14775, 2022. 1, 6, 7

[23] Jin Gao, Jialing Zhang, Xihui Liu, Trevor Darrell, Evan Shelhamer, and Dequan Wang. Back to the source: Diffusion-driven adaptation to test-time corruption. In *CVPR*, pages 11786–11796, 2023. 1, 2

[24] Shuaicheng Niu, Chunyan Miao, Guohao Chen, Pengcheng Wu, and Peilin Zhao. Test-time model adaptation with only forward passes. In *ICML*, 2024. 1, 2

[25] Yun-Yun Tsai, Fu-Chen Chen, Albert YC Chen, Junfeng Yang, Che-Chun Su, Min Sun, and Cheng-Hao Kuo. Gda: Generalized diffusion for robust test-time adaptation. In *CVPR*, pages 23242–23251, 2024. 1, 2

[26] Malik Boudiaf, Romain Mueller, Ismail Ben Ayed, and Luca Bertinetto. Parameter-free online test-time adaptation. In *CVPR*, pages 8344–8353, 2022. 1

[27] Adilbek Karmanov, Dayan Guan, Shijian Lu, Abdulmotaleb El Saddik, and Eric Xing. Efficient test-time adaptation of vision-language models. In *CVPR*, pages 14162–14171, 2024.

[28] Yu Sun, Xiaolong Wang, Zhuang Liu, John Miller, Alexei Efros, and Moritz Hardt. Test-time training with self-supervision for generalization under distribution shifts. In *ICML*, pages 9229–9248, 2020.

[29] Yuejiang Liu, Parth Kothari, Bastien Germain van Delft, Baptiste Bellot-Gurlet, Taylor Mordan, and Alexandre Alahi. Ttt++: When does self-supervised test-time training fail or thrive? In *NeurIPS*, volume 34, pages 21808–21820, 2021. 1

[30] M Jehanzeb Mirza, Inkyu Shin, Wei Lin, Andreas Schriebl, Kunyang Sun, Jaesung Choe, Mateusz Kozinski, Horst Possegger, In So Kweon, Kuk-Jin Yoon, et al. Mate: Masked autoencoders are online 3d test-time learners. In *ICCV*, pages 16709–16718, 2023. 1, 2, 5, 6, 7, 8

[31] Yanshuo Wang, Ali Cheraghian, Zeeshan Hayder, Jie Hong, Sameera Ramasinghe, Shafin Rahman, David Ahmedt-Aristizabal, Xuesong Li, Lars Petersson, and Mehrtash Ha-

randi. Backpropagation-free network for 3d test-time adaptation. In *CVPR*, pages 23231–23241, 2024. 1, 2, 6, 7, 8

[32] Hajin Shim, Changhun Kim, and Eunho Yang. Cloudfixer: Test-time adaptation for 3d point clouds via diffusion-guided geometric transformation. In *ECCV*, 2024. 2, 6, 7, 8

[33] Hamidreza Dastmalchi, Aijun An, Ali Cheraghian, Shafin Rahman, and Sameera Ramasinghe. Test-time adaptation of 3d point clouds via denoising diffusion models. In *WACV*, 2025. 2, 6, 7, 8

[34] Jonathan Ho, Ajay Jain, and Pieter Abbeel. Denoising diffusion probabilistic models. In *NeurIPS*, volume 33, pages 6840–6851, 2020. 2

[35] Jiaming Song, Chenlin Meng, and Stefano Ermon. Denoising diffusion implicit models. In *ICLR*, 2021.

[36] Yang Song, Jascha Sohl-Dickstein, Diederik P Kingma, Abhishek Kumar, Stefano Ermon, and Ben Poole. Score-based generative modeling through stochastic differential equations. In *ICLR*, 2021. 2

[37] Mathieu Aubry, Ulrich Schlickewei, and Daniel Cremers. The wave kernel signature: A quantum mechanical approach to shape analysis. In *ICCVW*, pages 1626–1633, 2011. 2, 8

[38] Jiaxi Hu and Jing Hua. Salient spectral geometric features for shape matching and retrieval. *VC*, 25:667–675, 2009.

[39] Martin Reuter, Franz-Erich Wolter, and Niklas Peinecke. Laplace–beltrami spectra as 'shape-dna' of surfaces and solids. *CAD*, 38(4):342–366, 2006.

[40] Raif M. Rustamov. Laplace-beltrami eigenfunctions for deformation invariant shape representation. In *SGP*, 2007. 3

[41] Jian Sun, Maks Ovsjanikov, and Leonidas J. Guibas. A concise and provably informative multi-scale signature based on heat diffusion. *CGF*, 28(5):1383–1392, 2009.

[42] Yiqun Wang, Jianwei Guo, Dong-Ming Yan, Kai Wang, and Xiaopeng Zhang. A robust local spectral descriptor for matching non-rigid shapes with incompatible shape structures. In *CVPR*, pages 6231–6240, 2019.

[43] Martin Weinmann, Boris Jutzi, and Clément Mallet. Semantic 3d scene interpretation: A framework combining optimal neighborhood size selection with relevant features. *ISPRS Annals*, 2:181–188, 2014. 2, 8

[44] Jiachen Sun, Qingzhao Zhang, Bhavya Kailkhura, Zhiding Yu, Chaowei Xiao, Z Morley Mao, Ankit Goyal, Hei Law, Bowei Liu, Alejandro Newell, et al. Benchmarking robustness of 3d point cloud recognition against common corruptions. In *ICML*, 2021. 2, 5, 6

[45] Dong-Hyun Lee et al. Pseudo-label: The simple and efficient semi-supervised learning method for deep neural networks. In *ICMLW*, volume 3, page 896, 2013. 2, 6, 7

[46] Mohammad Fahes, Tuan-Hung Vu, Andrei Bursuc, Patrick Pérez, and Raoul de Charette. Poda: Prompt-driven zero-shot domain adaptation. In *ICCV*, pages 18623–18633, 2023. 2

[47] Jiachen Sun, Mark Ibrahim, Melissa Hall, Ivan Evtimov, Z. Morley Mao, Cristian Canton Ferrer, and Caner Hazirbas. Vpa: Fully test-time visual prompt adaptation. In *ACM MM*, pages 5796–5806, 2023. 2

[48] Ryan Gomes, Andreas Krause, and Pietro Perona. Discriminative clustering by regularized information maximization. In *NeurIPS*, volume 23, 2010. 5

[49] Yuan Shi and Fei Sha. Information-theoretical learning of discriminative clusters for unsupervised domain adaptation. In *ICML*, 2012. 5

[50] Mikaela Angelina Uy, Quang-Hieu Pham, Binh-Son Hua, Thanh Nguyen, and Sai-Kit Yeung. Revisiting point cloud classification: A new benchmark dataset and classification model on real-world data. In *ICCV*, pages 1588–1597, 2019. 5, 6, 7

[51] Ilya Loshchilov and Frank Hutter. Decoupled weight decay regularization. In *ICLR*, 2019. 5

[52] Dawei Zhou, Nannan Wang, Heng Yang, Xinbo Gao, and Tongliang Liu. Phase-aware adversarial defense for improving adversarial robustness. In *International Conference on Machine Learning*, pages 42724–42741. PMLR, 2023. 8

[53] Qidong Huang, Xiaoyi Dong, Dongdong Chen, Yinpeng Chen, Lu Yuan, Gang Hua, Weiming Zhang, and Nenghai Yu. Improving adversarial robustness of masked autoencoders via test-time frequency-domain prompting. In *ICCV*, pages 1600–1610, 2023.

[54] Donghun Ryou, Inju Ha, Hyewon Yoo, Dongwan Kim, and Bohyung Han. Robust image denoising through adversarial frequency mixup. In *CVPR*, pages 2723–2732, 2024. 8

[55] Songyang Zhang, Shuguang Cui, and Zhi Ding. Hypergraph spectral analysis and processing in 3d point cloud. *IEEE TIP*, 30:1193–1206, 2020. 8

[56] Siheng Chen, Dong Tian, Chen Feng, Anthony Vetro, and Jelena Kovačević. Fast resampling of three-dimensional point clouds via graphs. *IEEE TSP*, 66(3):666–681, 2017. 8

[57] Qianjiang Hu, Daizong Liu, and Wei Hu. Exploring the devil in graph spectral domain for 3d point cloud attacks. In *ECCV*, pages 229–248, 2022. 8

[58] Daizong Liu, Wei Hu, and Xin Li. Point cloud attacks in graph spectral domain: When 3d geometry meets graph signal processing. *IEEE TPAMI*, 2023. 8

[59] Yuehui Han, Jiaxin Chen, Jianjun Qian, and Jin Xie. Graph spectral perturbation for 3d point cloud contrastive learning. In *ACM MM*, pages 5389–5398, 2023. 8